JOURNAL OF GEOPHYSICAL RESEARCH, VOL. 108, NO. D20, 4646, doi:10.1029/2003JD003400, 2003

A global view of the molecular oxygen night airglow

Paul B. Hays, Julie F. Kafkalidis, and Wilbert R. Skinner
Department of Atmospheric, Oceanic, and Space Sciences, University of Michigan, Ann Arbor, Michigan, USA

Raymond G. Roble
National Center for Atmospheric Research, Boulder, Colorado, USA

Received 10 January 2003; revised 22 March 2003; accepted 15 July 2003; published 28 October 2003.

[1] The High-Resolution Doppler Imager on the Upper Atmosphere Research Satellite has observed the O_2 atmospheric band nightglow at extremely high spatial resolution of 50 km in the horizontal over much of Earth's surface. These observations of the oxygen nightglow are shown to be a good surrogate for atomic oxygen outflow from the thermosphere and subsequent recombination in the upper mesosphere. The distribution of enhanced airglow and recombination verify the previous observations that bright regions of the nightglow are associated with descending motion, where the tides are transporting atomic oxygen out of the thermosphere, and regions of decreased airglow are associated with ascending tidal motion. The detailed observations of the global airglow at a scale of 100 km present a much more complex picture, however. The tidally enhanced regions are extremely structured, with strong longitudinal and latitudinal variability in brightness and associated atomic oxygen recombination. These structured regions are persistent on a timescale of a day or more, with certain regions of the globe exhibiting enhanced airglow much of the time. These regions are present over the entire night side of the globe but are strongly modulated by the ascending and descending tidal motions. A theoretical study of these enhancements suggests that they are caused by the upward propagation of gravity waves, which break in the high mesosphere and induce strong vertical motion in the atmosphere. It is interesting that the primary cause of the increased transport of atomic oxygen is vertical motion rather than the conventional enhanced turbulence explanation. These gravity waves are associated with wind shear and strong convective activity in the troposphere and often appear in certain preferred locations where convective activity is expected. These observations have important implications for the basic processes by which momentum and energy are deposited in the upper mesosphere. We suggest that the processes must be modeled as stochastic events that dance around the base of the thermosphere, generally in climatologically preferred regions, rather than the relatively uniform distribution of gravity wave forcings that is being used in general circulation models up to this time. *INDEX TERMS:* 0310 Atmospheric Composition and Structure: Airglow and aurora; 0341 Atmospheric Composition and Structure: Middle atmosphere—constituent transport and chemistry (3334); 0355 Atmospheric Composition and Structure: Thermosphere—composition and chemistry; *KEYWORDS:* airglow, transport, structure, atomic oxygen, thermosphere

Citation: Hays, P. B., J. F. Kafkalidis, W. R. Skinner, and R. G. Roble, A global view of the molecular oxygen night airglow, *J. Geophys. Res.*, *108*(D20), 4646, doi:10.1029/2003JD003400, 2003.

1. Introduction

[2] The brightest spectral features in the nighttime airglow result from the recombination of atomic oxygen in the upper mesosphere. Among the most intense emissions created in this way are the O_2 atmospheric bands which result from the decay of the excited $O_2(b^1\Sigma_g^+)$ state to its ground electronic state, $O_2(X^3\Sigma_g^-)$ [*Chamberlain*, 1954]. The excited state is produced by the recombination of atomic oxygen with O_2 via the two-step Barth mechanism [*Greer et al.*, 1981; *McDade et al.*, 1986; *Murtagh et al.*, 1990]. The brightest of these bands, the (0,0) band, cannot be observed from the ground since it terminates in the ground state of molecular oxygen and thus is absorbed by the dense lower atmosphere; however, this very bright emission feature can be seen from space where individual rotational lines in the band appear on a dark spectral background due to absorption of light in the lower atmosphere. This intense $O_2(^1\Sigma)$ nightglow emission peaks at a nominal altitude of 94 km.

[3] The O_2 atmospheric band emission, like its companion $O(^1S)$ green line, is closely associated with the process of recombination of atomic oxygen that takes place in the

0148-0227/03/2003JD003400

upper mesosphere. In this region of the atmosphere atomic oxygen, which is created in the day by photo-dissociation of molecular oxygen in the thermosphere, recombines to complete the atmospheric oxygen cycle [*Kasting and Roble*, 1981]. The creation and destruction of atomic oxygen produces the vast thermospheric atomic oxygen reservoir, which varies relatively gradually over the surface of Earth. The outflow and subsequent recombination of atomic oxygen is, however, very structured, having strong variation with latitude, local time, and even longitude. These variations are due to the existence of tides, waves, and turbulence that modulate the downward transport of atomic oxygen into the upper mesosphere where recombination occurs. These processes can be studied by observing the associated variations in the O_2 atmospheric band brightness over the surface of Earth.

[4] Most previous studies of structures in the airglow have been made from the ground where only a relatively small region, of at most hundreds of kilometers across, can be observed at one time. These studies have revealed the existence of gravity waves with scales of tens of kilometers [e.g., *Taylor et al.*, 1995]. The relationship between the small-scale gravity wave perturbations seen in the airglow and the global scale of oxygen recombination is at best tenuous. Temporal variations of airglow features observed from the ground hint at the existence of much larger-scale processes that are related to global oxygen transport, but time and space are easily confused when observing the airglow. Processes such as tidal oscillations, large-scale gravity waves and magnetic storm events make it difficult to determine whether one is observing a migrating spatial feature or some process that is merely varying with time.

[5] The global-scale structure in the airglow is best observed from space. Previous satellite observations of the mesospheric nightglow emissions had a horizontal resolution of 500 km or larger. Images of the O_2 atmospheric bands with a pixel resolution of about 50 km have been obtained from the High-Resolution Doppler Imager (HRDI) on the Upper Atmosphere Research Satellite (UARS) between the years of 1996 and 2000. By studying these high-resolution global images of the O_2 atmospheric band airglow created during the recombination process, we examine this global outflow of atomic oxygen from the thermosphere on scales hitherto unobserved.

2. Previous Global Airglow Observations

[6] Early observations of spatial structure in the nocturnal mesospheric airglow were obtained from the ground [*Dufay and Tcheng*, 1946; *Ward and Silverman*, 1962; *Silverman*, 1964]. Later, observations from stations at a range of latitudes [e.g., *Brenton and Silverman*, 1970; *Fukuyama*, 1976; *Petitdidier and Teitelbaum*, 1979; *Takahashi et al.*, 1977, 1984, 1985] suggested that these variations were mainly due to global-scale solar tidal forcing. A truly global view of the airglow structure only became possible with the advent of satellite techniques. The first mesospheric study was made with data from the OGO-6 satellite, which obtained information on the spatial morphology of the $O(^1S)$ 557.7-nm emission [*Thomas and Donahue*, 1972]. This investigation was extended by *Donahue et al.* [1974], who deduced strong variations of the atomic oxygen density with space, time, and season from these nightglow measurements. *Petitdidier and Teitelbaum* [1979] and *Akmaev and Shved* [1980] attempted to simulate the tidal behavior in the 557.7-nm nightglow, and concluded that tidal-induced vertical motions drove the phenomenon.

[7] Local time variations over a small range of latitudes were addressed by *Yee and Abreu* [1987] with AE-E satellite measurements of the $O(^1S)$ nightglow for equinox conditions. These observations indicated dominant components at a period of 10–12 hours for latitudes of 10°–20°, while wave structures of much shorter timescales were found near the equator. The AE-E investigation was limited by local time coverage, latitude range, and the size of the data set.

[8] The observations that will be discussed here were taken with HRDI on UARS. This instrument is a Fabry-Perot interferometer designed to observe the $O_2(0,0)$ band emission lines at the extremely high spectral resolution required to measure the wind, temperature, and pressure in the atmosphere using the spectral shifts, broadening, and intensity of individual rotational lines [*Hays et al.*, 1993; *Grassl et al.*, 1995]. The early HRDI observations are of limited spatial resolution because the primary goal has been to measure the wind using the interferometer in the Doppler mode. The Doppler mode requires relatively long integration times at night, with which a wind vector measurement is normally obtained about every 5° of arc parallel to the orbit of UARS. Along with these wind measurements, HRDI has obtained low-resolution observations of the global distribution of the intensity of mesospheric emissions [*Burrage et al.*, 1994; *Yee et al.*, 1997; *Skinner et al.*, 1998; J. H. Yee et al., Retrievals of atomic oxygen distribution in the mesosphere and lower thermosphere (85–105 km), submitted to *Journal of Geophysical Research*, 2003, hereinafter referred to as Yee et al., submitted manuscript, 2003]. The Wind Imaging Interferometer (WINDII) on UARS [e.g., *Shepherd et al.*, 1993a, 1997] has conducted very similar studies by observing the atomic oxygen green line at 557.7 nm. All of these observations, although of modest spatial resolution, have shown the existence of a great deal of structure in the mesospheric airglow. *Burrage et al.* [1994] related a global-scale variation in the observed night O_2 atmospheric band brightness to the (1,1) diurnal tide. In the equatorial regions, the $O_2(0,0)$ emission is enhanced in the early evening hours. By early morning, this tidal enhancement has shifted to the midlatitudes, and the equatorial region reaches a minimum brightness. This tidal pattern persisted throughout the two years examined. The largest amplitude enhancements occurred during spring equinox, when the tidal amplitude is maximum. Weaker variations were observed at both solstices. A similar behavior was identified in WINDII $O(^1S)$ and OH(8,3) observations [*Shepherd et al.*, 1995; *Zhang and Shepherd*, 1999] and HRDI observations of vertically resolved $O(^1S)$, OH(9,4) and $O_2(0,0)$ [*Skinner et al.*, 1998], which also revealed the altitude structure of the phenomenon. *Marsh et al.* [1999] found similar behavior in the O_2 atmospheric band dayglow.

[9] The basic mechanisms producing the tidal variations in the nightglow emissions are now fairly well understood. *Shepherd et al.* [1995] observe that the equatorial peak in the $O(^1S)$ emission layer descends from 95 km to 89 km

during the evening hours, where it weakens around midnight, then reappears at a high altitude and increases in intensity throughout the morning hours. They relate this behavior to the tidally induced density and wind perturbations predicted by the *Forbes* [1982a, 1982b] tidal model, suggesting the evening descent in the emission layer results from a similarly descending tidal enhancement in neutral density, with associated tidal variations in the atomic oxygen mixing ratio also playing a role. More recently, the latitude/altitude/local time variations in the brightness of all three nightglow emissions [$O_2(^1\Sigma)$, $O(^1S)$, and OH] have been simulated with the TIME-GCM [*Yee et al.*, 1997] and the results compared with observations. This study demonstrated the important role of vertical motions in changing the atomic oxygen concentration, with downward motion increasing [O] and enhancing the airglow brightness, and upward motion having the reverse effect. The latitude structure of [O] is related to latitudinal variations in vertical transport set up by meridional circulations in the thermosphere. For example, [O] is enhanced by subsidence at the high latitudes during the winter solstice. This basic latitudinal structure varies seasonally, but is also strongly modulated by the daily tidal cycle. Vertical motions produced by the tides are shown to account for the observation of the inverse relationship between the altitude of the peak emission and the column-integrated brightness, with downward motion of atomic oxygen again enhancing the emission brightness and moving the peak emission to a lower altitude. *Ward* [1998] has investigated this causal relation by tracking the vertical motions of air parcels in the tidal wind fields generated by the Global Scale Wave Model [*Hagan et al.*, 1995]. He concludes the emission rate variations are due to the tidally induced epicyclical motion of air parcels, and again attributes latitudinal variations in airglow to tidal variations in the vertical velocity with latitude. Unlike *Forbes* [1982a, 1982b], who suggested density perturbations played the dominant role, *Ward* [1998] shows that it is the tidally driven vertical advection which produces the dominant variation in emission brightness, whereas the brightness variations resulting from tidally driven temperature and density changes are exactly out of phase with this dominant advective component.

[10] If the spatial morphology of an emission is determined purely by migrating tides, then on a single day the airglow brightness would appear from UARS to be zonally uniform since the orbit precesses very slowly in local time. *Burrage et al.* [1994] found very large longitudinal variations in daily global brightness maps, and suggested that these might result from the modulation of the tidal structure by planetary waves. Longitudinal structures have also been detected in WINDII $O(^1S)$ nightglow data [*Shepherd et al.*, 1993b, 1999], and in particular *Ward et al.* [1997] detected the signature of a two-day wave. All of the studies discussed above have focused on planetary-scale phenomena, due to the relatively low spatial resolution of previously available satellite airglow observations.

[11] It is clear that significant large-scale temporal, latitudinal, and longitudinal variations are present in each of the nightglow emissions previously observed, which implies that the recombination of atomic oxygen is similarly structured. Our understanding of these airglow structures and the underlying recombination of atomic oxygen has been limited heretofore by the scale and spatial resolution of the previous satellite observations.

3. HRDI High-Resolution Airglow Imaging Mode

[12] Early in 1996 a new mode of operation of HRDI was initiated that provides a global view of the nighttime oxygen airglow at very high spatial resolution. This mode makes use of the photometer that is part of the HRDI instrument [*Hays et al.*, 1993; *Grassl et al.*, 1995]. The photometer is much more sensitive to the brightness of the O_2 atmospheric bands than the interferometer and thus allows observations to be collected at the shortest possible integration time of 0.096 s at a sampling rate of one integration every 0.128 s. The telescope is used in this imaging mode as a raster scanner. The line of sight is swept in a scan at a fixed zenith angle of 67° such that the tangent altitude is kept constant at 32 km, as illustrated in the bottom of Figure 1. The telescope azimuth angle is then slewed back and forth continuously between +55° and −55° (where 0° azimuth is along the spacecraft x axis, parallel (antiparallel) to the spacecraft velocity vector during forward (backward) flight) causing the line of sight to sweep over the surface of Earth, sampling the airglow brightness over a 3200-km-wide swath centered on the orbit track. Since the airglow layer is thin, the telescope field of view (1.369° in the horizontal by 0.120° in the vertical) intersects only a small rectangular region of the layer as shown in the top of Figure 1. The area of the airglow layer viewed by the instrument under these viewing conditions has an instantaneous "footprint" of approximately 30 km × 40 km in the horizontal. The spacecraft's forward motion advances this cross-track scan along the orbit, completing the raster effect. Each 110° azimuthal slew takes about 10–11 s, yielding a cross-track spacing between measurements of about 40 km, so adjacent measurements overlap in the cross-track direction. The forward velocity of UARS advances the measurements by approximately 70 km in the center of the swath, with about 140 km between the turnaround positions at the edges of the swath. A more detailed discussion of the scan process and data processing will be provided in a future publication by J. Kafkalidis (manuscript in preparation, 2003).

[13] The telescope line of sight intersects the airglow layer in two places. Because molecular oxygen in the lower atmosphere self-absorbs the emission lines being viewed, only the airglow coming from the intersection point nearest to the spacecraft is seen. By contrast, when optically thin features such as the oxygen green line or hydroxyl lines are viewed in this geometry, both intersection points are seen simultaneously. In that case, the result can be quite confusing since the two intersection points are spaced apart by as much as 17° of angular separation.

[14] An example of the detailed pixel-by-pixel raster scan is shown in Figure 2. We note in Figure 2 that strong signal variations are observed on scales as short as 100 km. The signal levels shown here are raw counts per integration period and, as a consequence, the signal-to-noise obeys simple Poisson statistics. In general the signal-to-noise ratio varies from about 5:1 to 20:1 in these raw

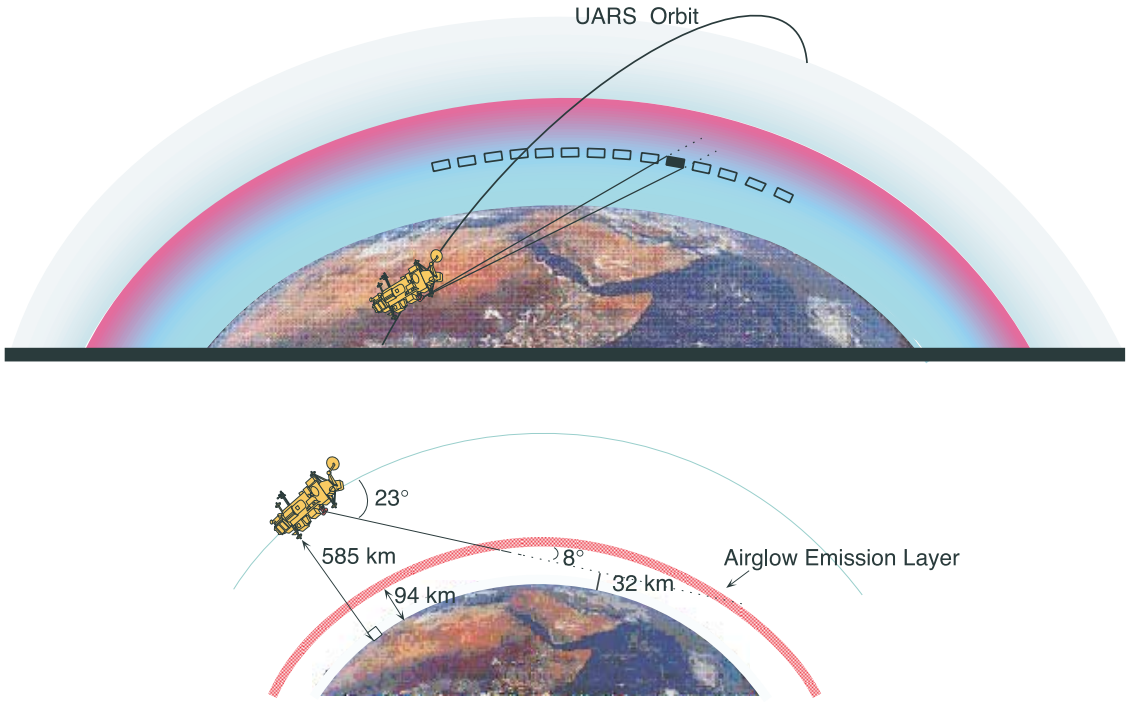

Figure 1. Schematic depiction of HRDI high-resolution observational geometry. (top) With each side-to-side (cross-track) slew of the telescope, the measurement footprint (30 km × 40 km in size) sweeps out a 3200-km-wide swath. Many more individual samples (between 78 and 86 per slew) are collected within the swath than are shown here, and adjacent samples actually overlap in the cross-track direction. (bottom) The telescope elevation angle is held constant at 23° to achieve a constant tangent altitude of 32 km. The line-of-sight path, which penetrates the airglow layer at a glancing angle of 8°, actually intersects the airglow layer at two places, but only the intersection nearest the spacecraft is viewed because emissions from the farther intersection are self-absorbed by the intervening lower atmosphere.

images. The instrument electronic background is typically only 2–3 counts except when UARS encounters a high density of precipitating energetic electrons, which happens in the South Atlantic Anomaly region and on occasion when flying through the auroral zones.

[15] The conversion from raw counts to atmospheric (0,0) band brightness is accomplished by noting that the background dark count from the photometer is very small, and transforming from counts to brightness by multiplying by a calibration factor which depends on the source region temperature and instrument characteristics. The images that will be shown in the remainder of this paper will be converted to equivalent layer brightness in Rayleighs with twilight, auroral, moon, and spacecraft-scattered sunlight removed. These four sources of contamination in the airglow signal occur under easily recognized and repeatable conditions, and the small amount of data affected are flagged as unusable. For example, the spacecraft-scattered sunlight (glint) occurs only near dawn and dusk while UARS is still illuminated by sunlight, when for azimuth angles near 0° sunlight reflected from a support post on the bottom side of UARS is able to enter the HRDI telescope line-of-sight path. Once the solar zenith angle of UARS exceeds 114°, UARS is in shadow and this glint disappears. The removal of these anomalous features and conversion of the raw counts to band brightness will be discussed in more detail in a future publication by J. Kafkalidis (manuscript in preparation, 2003).

4. Global Images of the March/April Equinox O_2 Nightglow

[16] The HRDI high-resolution images that will be examined here are taken during a month-long period in March–April of 1998, extending from 17 March to 14 April. The latitude/local time dependence in the brightness from the March–April time period is shown in Figure 3. As the raster scan images a swath of airglow, the longitudinal extent of the swath at each latitude dictates the range of local times being sampled. To form Figure 3, the data collected in March and April are binned into a grid of size 2° in latitude by 6 min (0.1 h) in local time, and all the data within each bin are averaged together. Each bin space shown contains at least 50 individual measurements, and the vast majority of bin spaces contain about 750 individual measurements collected over at least 2–4 consecutive nights. Because the same bin space will be sampled on all 15 orbits (15 longitudes) on a given day, this latitude/local time binning and averaging is equivalent to zonally averaging the raw image data collected within each latitude/local time bin. For a single night, the local time coverage of an individual orbital swath spans approximately 2 hours at the

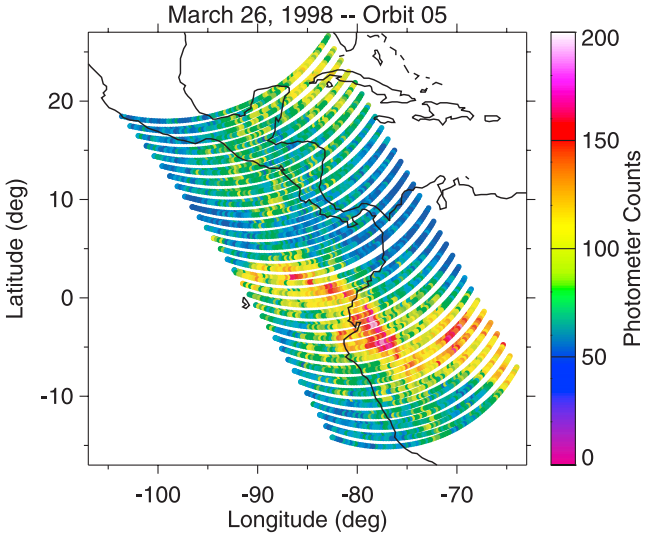

Figure 2. HRDI raster pattern showing an 11-min segment of data comprised of 5162 individual samples (integrations). The dots mark the exact centroid location of each sample, but the dot size is somewhat larger than the actual measurement "footprint." The raster scan is interrupted briefly once every 5.5 min to perform a short calibration sequence, which creates the small data gap (barely visible) in the middle of this segment. The photometer counts are multiplied by a combined calibration and geometric factor of 110 Rayleighs/count to convert the raw signal in counts (which is integrated in the line-of-sight direction) into the O_2 band brightness in Rayleighs (integrated in the zenith direction).

equator and a much wider and more variable range of 4–8 hours at the higher latitudes. The orbital precession shifts this nightly coverage to progressively earlier local times at a rate of 20 min/day. During March, UARS was in forward flight and the northern latitudes were sampled first in the early evening on the ascending node of the orbit, and then in the morning on the descending node. On 2 April, UARS performed a yaw-around maneuver from forward to backward flight, so during April the descending node of the orbit sampled the evening hours and the ascending node the morning hours. This behavior is related to the precession of the orbital plane, with the descending node moving in retrograde from morning in mid-March to evening in the middle of April 1998.

[17] The brightness variations seen in Figure 3 are nearly identical to those shown in the work of *Burrage et al.* [1994], which have been related to tidally induced descending motions that transport atomic oxygen downward from the thermospheric reservoir into the upper mesosphere [*Yee et al.*, 1997; *Ward*, 1998, 1999]. Here the evening exhibits enhanced brightness where the (1,1) tide is descending along the equator, only to be replaced in the morning by enhancements extending from 20° to 40° latitude because the tidal decent in the midlatitudes is shifted in phase by several hours from that at the equator. It is interesting to note that in both the February–April 1993 equinox data shown in the work of *Burrage et al.* [1994] and the present March–April 1998 brightness maps, there is a clear asymmetry between the Northern and Southern Hemispheres. Both in 1993 and 1998 this asymmetry is exhibited by the southern morning midlatitude enhancement being brighter and beginning much earlier in local time. This same asymmetry is consistently seen in all equinox seasons in which HRDI O_2 nightglow data have been collected, with the fall hemisphere morning enhancement being brighter and beginning earlier than that of the spring hemisphere (G. Fall, Morphology and interpretation of the O_2 atmospheric band nightglow as observed by the High-Resolution Doppler Imager, Ph.D. thesis, in preparation, 2003).

4.1. March/April Equinox Morning

[18] The discussion of the individual global brightness distribution begins with an image of the O_2 nightglow obtained on 22 March as shown in Figure 4. This and all subsequent global maps are formed by combining the raw data points from all 15 orbits in a 24-hour period, binning and averaging them in a 0.75° × 0.75° longitude-latitude grid. Typically, three to four data points are averaged within each grid cell. To ensure that data from two very different local times are not averaged together within the same grid cell, only the descending node data are included in Figure 4 and subsequent daily maps.

[19] The most striking features in the nightglow during the Northern Hemisphere spring equinox period of March 1998 are very large-scale, bright patches appearing against a more quiescent background and distributed in longitude within the two midlatitude bands from 20° to 40°. The position in latitude of these bright features is consistent with the tidally induced variations previously discussed. What is remarkable, surprising even, is the strong longitudinal structure present within these midlatitude tidal bands. If the diurnal tides were the only influence on the airglow brightness, one would expect to see uniformly bright bands centered on 30°N and 30°S, as is predicted by theory [e.g., *Yee et al.*, 1997]. The images are extremely patchy, however, with large regions of high brightness followed by adjacent regions of very low brightness. In form, these patches remain coherent on timescales of a few hours, since

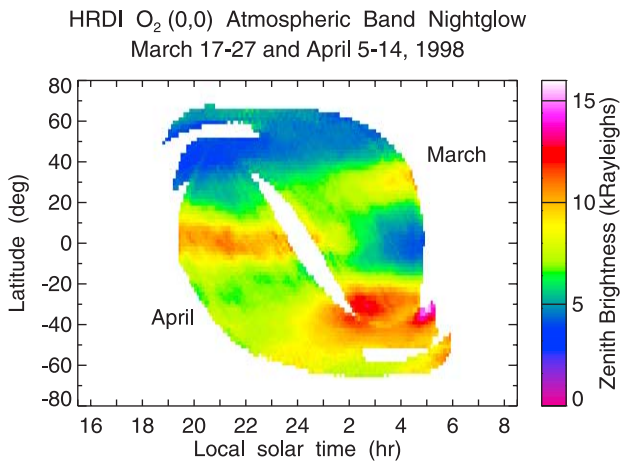

Figure 3. March–April 1998 latitude versus local time O_2 brightness map. The data included in this map are from all 21 days observed during these two months, 17–27 March and 5–14 April.

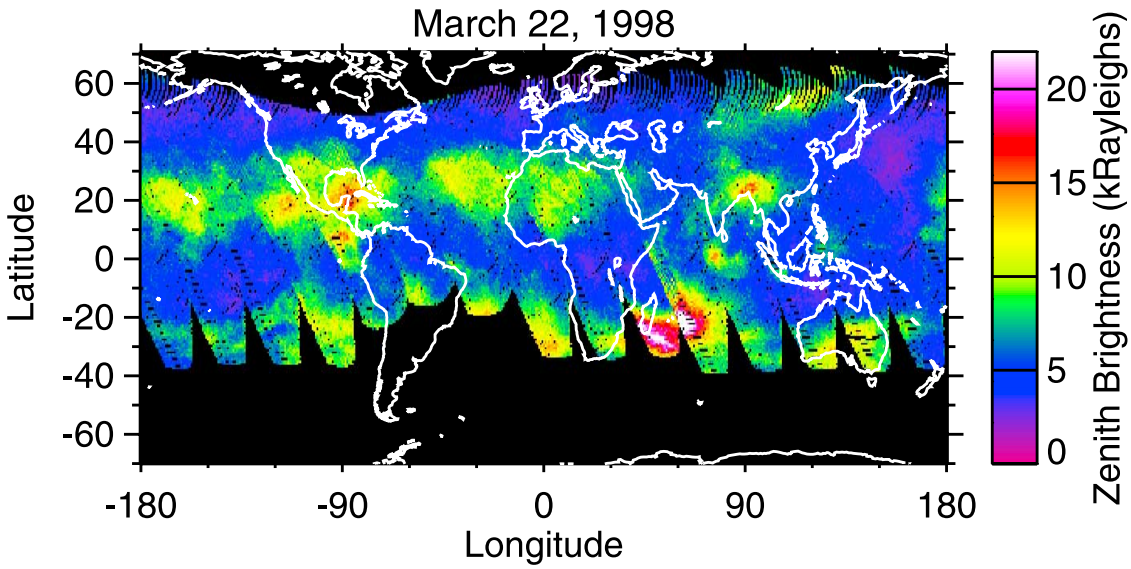

Figure 4. O_2 atmospheric band nightglow for 22 March 1998. This map is a 24-hour composite of data from all 15 orbits on that day. Only data from the descending node of the orbit are included, and the local time coverage is mostly in the morning hours. The coverage starts at 2306 LT at 66°N, and extends to the edge of morning twilight in the Southern Hemisphere, ranging over 0400–0436 LT at 39°S. Data have been discarded within the South Atlantic Anomaly region and northern auroral zone.

the shape defining a bright region does not appear to change significantly in the 97-min interval in UT between two consecutive orbits. These large-scale patterns do evolve significantly in the 24 hours it takes the satellite view to return to the same region on the globe. The bright feature just east of Madagascar illustrates the very large changes that can happen over a 24-hour period. The discontinuity in this bright feature is at the day boundary where the first and last orbits in the day (separated by 22.6 hours) meet. There are bright features that persist over the same location for as long as several days. The enhancement over the Gulf of Mexico in this figure is such a long-lived bright feature, and is at the same location where a persistent bright feature was identified by *Burrage et al.* [1994] in data from 1992 to

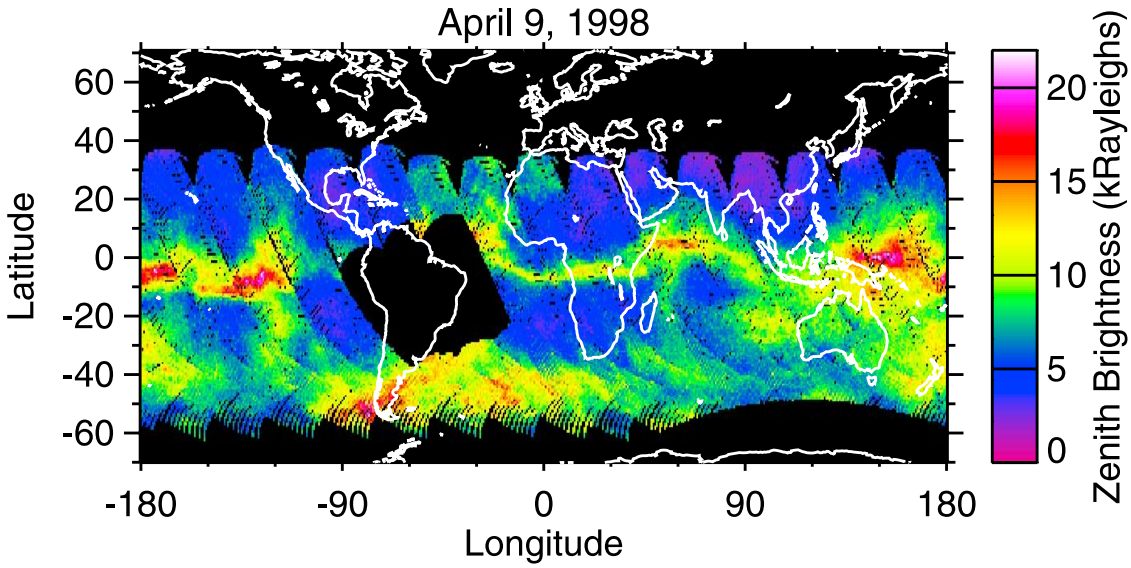

Figure 5. O_2 atmospheric band nightglow for 9 April 1998. This map is a 24-hour composite of data from all 15 orbits on that day. Only data from the descending node of the orbit are included, and the local time coverage is mostly in the evening hours. The coverage starts along the edge of evening twilight in the Northern Hemisphere, ranging over 2024–2048 LT at 38°N, and extends to 0230 LT at 63°S. Data have been discarded within the South Atlantic Anomaly region and southern auroral zone.

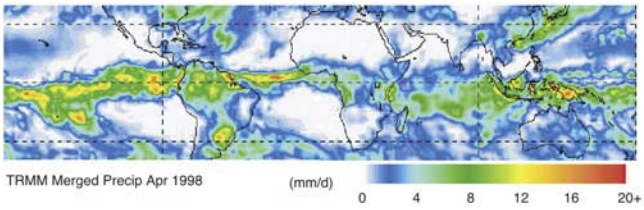

Figure 6. April 1998 Tropical Rainfall Measuring Mission (TRMM) satellite measurements of rainfall rate, from which the Intertropical Convergence Zone location can be inferred. (Figure and monthly precipitation data for April 1998 are available from the World Wide Web at http://trmm.gsfc.nasa.gov.)

1993. The longitudinal structure seen in these spring equinox data suggests the same kind of low-order planetary-wave variations previously identified in WINDII and HRDI data [*Shepherd et al.*, 1993b; *Ward et al.*, 1997; Yee et al., submitted manuscript, 2003].

4.2. March/April Equinox Evening

[20] In April the UARS orbit has processed to the point where the descending leg of the orbit passes through the evening hours (Figure 5). Gone are the continental-scale bright patches seen in early morning during March; here the early evening equatorial tidal enhancement is confined to a surprisingly narrow, sinewy region. As was true during spring equinox in the Northern Hemisphere midlatitudes, significant longitudinal structure is superposed on this equatorial tidal enhancement, but the April evening bright features are much smaller and more filigreed in appearance than the morning midlatitude features observed in March. The evening equatorial enhancement wanders between 10°S and 10°N with strong longitudinal modulations in integral brightness. Certain regions are always relatively bright, with the Indonesian area being noteworthy. The width of the equatorial bright band is variable, ranging from a few degrees wide to as much as 20° wide at places. This width is somewhat subjective since the brightness varies so markedly.

[21] The contorted shape of this equatorial band is suggestive of the location of the Intertropical Convergence Zone (ITCZ). Figure 6 shows the April 1998 Tropical Rainfall Measuring Mission (TRMM) rainfall rate, which maximizes along the ITCZ. Certain features of the April equatorial nightglow enhancement follow the region of high rainfall in rather great detail. This might be expected since the ITCZ is a region of greatly enhanced convection induced by the Hadley circulation. This region is the source of a great deal of gravity wave activity.

4.3. Morning to Evening Transition

[22] The two illustrations that have just been discussed are extremely interesting in themselves, but the complete series of brightness images demonstrates a degree of complexity that is also of great interest. Figure 7 is a composite of 21 days of nightglow data taken as the satellite orbit precessed from dawn through early evening. The zonal average behavior of the brightness during this progression is seen in the latitude/local time chart shown in Figure 3. We note in the composite that on the first day, 17 March 1998, shown in the upper left-hand corner of Figure 7, the tidal enhancement is confined to a relatively uniform band centered between 20°N and 40°N. This band has significant longitudinal structure with three main centers of enhanced recombination, one over the Gulf of Mexico, one over Africa, and a third over eastern Asia. On this day the orbit passes through the twilight line at a point that eliminates all nighttime observation of the Southern Hemisphere.

[23] In the days that follow, the morning tidal downwelling at midlatitudes in the Northern Hemisphere appears to moderate with the bright nightglow patches becoming less bright and breaking up into a more irregular band. By 20 March, the southern midlatitude tidal band is being sampled near morning twilight. There is a significant time difference between the northern and southern crossings of the respective morning tidal bands. The southern morning band is brighter than the northern band. Note in Figure 3 that the northern midlatitude morning enhancement appears quite dim before about 0300 LT, but is still present as scattered bright patches in the individual daily maps on 23 March and later days (from 23 March forward, the Northern Hemisphere poleward of 20° is only sampled at local times earlier than 0300 LT). The evening equatorial enhancement actually extends to about 0100–0200 LT, and appears in the data sampled on the days following 23 March. This is also seen in Figure 3 where observations just after midnight exhibit peaks in both the midlatitudes and at the equator.

[24] There is an eight-day gap in the observations, from 28 March through 4 April. During the April sequence (5–14 April), the descending node sweeps through the equator in the evening. The equatorial evening tidal enhancement in recombination is a dominant feature of the maps throughout the April sequence. The evening equatorial enhancement is relatively constant when viewed as a longitudinal average in Figure 3, but is extremely structured when viewed on the individual daily maps. There are interesting structures in the equatorial tidal feature that repeat on many of the days. In the eastern Pacific Ocean, the bright region bends sharply northward from south of the equator to about 10°N as one follows the enhancement eastward just west of Central America. The path of the equatorial enhancement dips southward across Africa, swings northward over the Bay of Bengal, then back southward over Southern Asia with a very consistent bright region over Indonesia. These relatively consistent features are present in nearly all of the evening equatorial maps that have been examined in other equinox seasons for other years (not shown) as well as March/April 1998. There are great variations in the brightness along the equatorial enhancement, however, with features appearing and disappearing between one 24-hour composite map and the next. The bright features do appear to have continuity over one orbital period, but from day to day there is a great variation in the recombination rate as seen in the O_2 atmospheric band brightness.

[25] Note that the nightside view of the Northern Hemisphere is lost as the orbit precesses into the evening twilight, crossing into day in the north. As the April sequence proceeds, the day-night crossing moves equatorward, until by 14 April only latitudes south of 20°N are sampled on the night side. In this April sequence, there is a very bright high southern latitude band starting around midnight, appearing on any given night between about 2300 LT and 0100 LT. This band lies between 40°S and 60°S latitude, where tidal

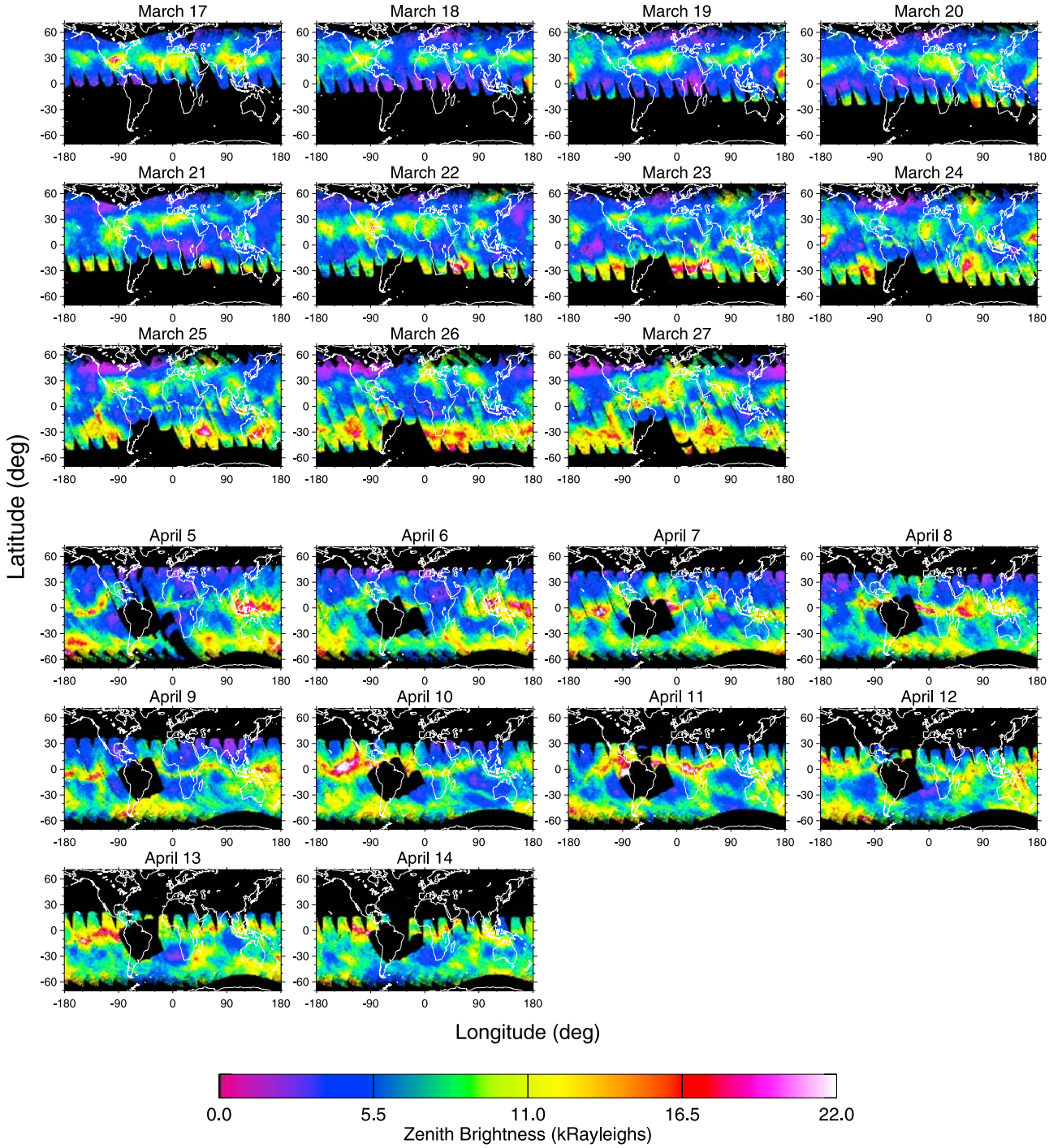

Figure 7. March–April 1998 composite of daily O_2 atmospheric band brightness maps.

downwelling would not appear to be of much consequence. This high-latitude enhancement also exhibits extreme longitudinal structure. Throughout 5–11 April, the southern midlatitudes between 20°S and 40°S are sampled only on the descending leg of the orbit and always prior to 0300 LT, therefore the morning midlatitude tidal enhancement in the Southern Hemisphere is not imaged during this April sequence. (Only on 12–14 April do the midlatitudes begin to be viewed on the ascending leg of the orbit as well, in the morning hours of 0300–0600 LT.) A shorter sequence of global images from the end of April (not shown) which does sample the southern midlatitudes in the morning shows that the morning southern midlatitude tidal band, first seen during 21–27 March, continues to be very bright, as expected for the fall equinox season. This southern band contains large-scale longitudinal structures similar to the large patches seen in the Northern Hemisphere morning tidal band during March. Both throughout 21–27 March and again in late April, the southern midlatitude patches do not appear to be quite as isolated as in the Northern

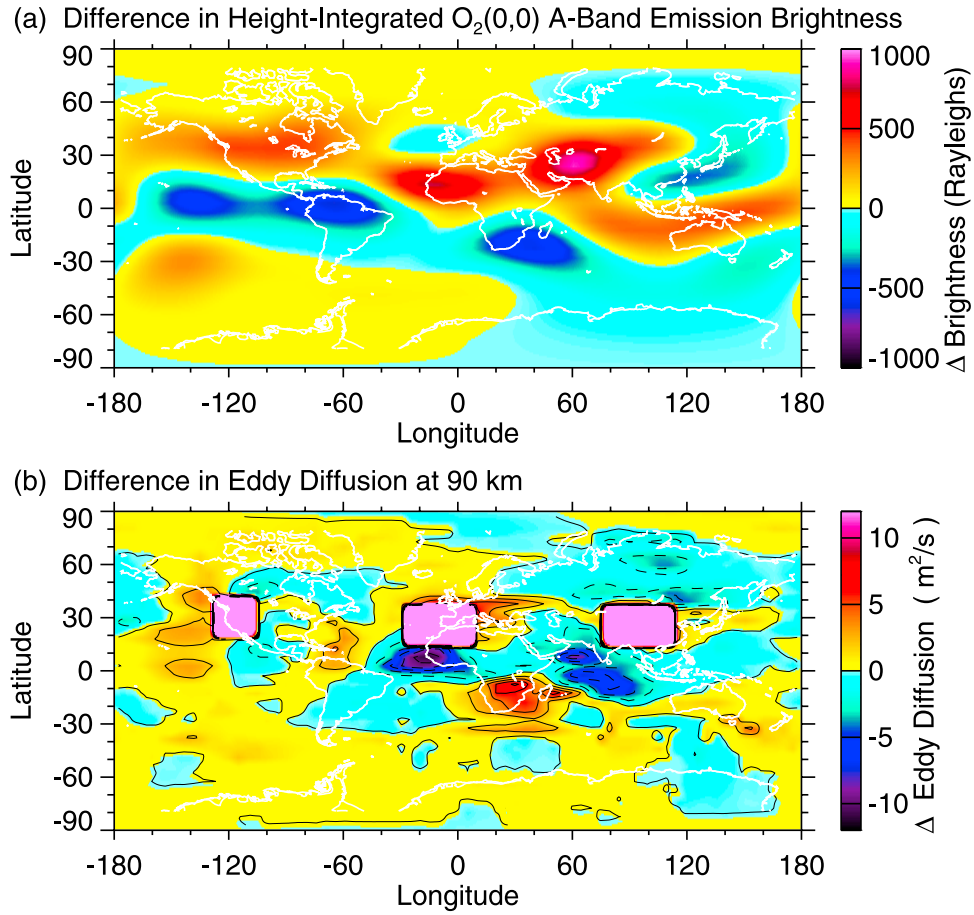

Figure 8. A TIME-GCM run with locally enhanced gravity wave forcing (perturbed case) is compared to the base run with a uniform gravity wave source function. Both runs simulate perpetual March equinox conditions. (a) Difference (perturbed minus base) in height-integrated O_2 emission brightness. (b) Difference (perturbed minus base) in eddy diffusion at 90 km altitude. In the regions where the gravity wave forcing was enhanced (pink rectangles), the eddy diffusion difference field reaches 54.9 m^2/s. Outside these regions of imposed enhanced forcing, the eddy diffusion difference field ranges from

Hemisphere. In the late April sequence, the midlatitude bright regions also seem to merge with the strong enhancements evident in the high southern latitudes throughout April. Similar large-scale enhancements which appear to connect or continue across a wide range of latitudes have also been seen in the Northern Hemisphere middle to high latitudes and spanning the low to middle latitudes, sometimes crossing the equator. Features which span such a wide range of latitudes also span a range of local times in the HRDI view of the world, therefore these large, connected features appear to be nontidal in origin.

5. Transport Processes and the O_2 Atmospheric Band Brightness

[26] What is seen in the composite shown in Figure 7, and in all of the maps examined previously, is consistent with the tidal forcing that has been discussed in earlier studies of the global distribution of the nightglow [*Burrage et al.*, 1994; *Ward*, 1998, 1999; Yee et al., submitted manuscript, 2003]. The airglow variations resulting from tidal motions are most evident in the longitudinally averaged data (Figure 3), whereas on an individual day the tidal pattern is often obscured by the longitudinal structure of the brightness. This large geographic variability in the patterns of the airglow would appear to demonstrate that there is extreme variability in the processes that transport atomic oxygen from the thermosphere into the mesosphere where recombinational chemistry occurs. These processes include both downwelling and turbulence, which are nearly indistinguishable in any airglow observation. Little has been known about the spatial and temporal distribution of these processes, but the HRDI high-resolution observations can be used to better observe the vagaries of downward transport of atomic oxygen out of the thermosphere.

5.1. Time-GCM Simulation of Airglow Patches

[27] In an attempt to better understand the airglow observations, the NCAR Thermosphere-Ionosphere-Mesosphere-Electrodynamics General Circulation Model (TIME-GCM) is used to simulate tide and gravity wave influences on the airglow emissions. The model has been used previously to examine tidal and seasonal influences of dynamics on airglow structure for equinox and solstice conditions [*Yee et al.*, 1997; *Roble and Shepherd*, 1997; *Shepherd et al.*, 1998; *Roble*, 2000; *Zhang et al.*, 2001; *Liu et al.*, 2001].

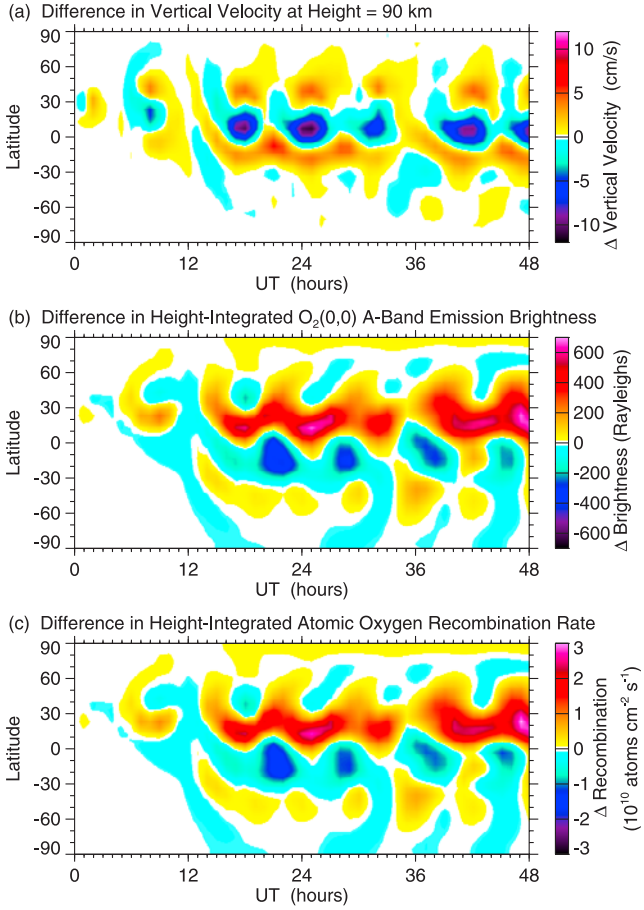

Figure 9. Universal time evolution over two days of the difference fields for (perturbed minus base) TIME-GCM runs (see text and Figure 8), at a local solar time of midnight: (a) difference in vertical velocity at 90-km altitude, (b) difference in height-integrated O_2 emission brightness, (c) difference in height-integrated O recombination rate.

These simulations primarily addressed the large-scale influences of tidal and planetary waves on airglow and not the small-scale features. Here we use the TIME-GCM in a series of simulations to examine the influence of gravity wave perturbations on airglow that would be superimposed on any larger-scale forcings.

[28] The TIME-GCM is a global model of the upper atmosphere from 30 to 500 km altitude that has been described by *Roble and Ridley* [1994] with recent updates given by *Roble* [1995, 2000]. The model is on a 5° latitude-by-longitude grid with 4 grid points per scale height extending between 30 and 500 km and uses a 5-min time step. The model cannot resolve many of the small-scale features observed by the HRDI instrument operating in its high-resolution mode but it can address the regional airglow variations seen in the data.

[29] For the simulations the solar radiative forcing (F10.7 = 150) and auroral forcing (cross polar cap potential drop of 45 KV and aurora hemisphere power input of 16 GW) are held constant. At the lower boundary of the model of 10 mbar, the tides are specified from the Global Scale Wave Model (GSWM) [*Hagan*, 1996] in addition to the zonally averaged geopotential height and temperature from the empirical model of *Fleming et al.* [1988]. The only parameter varied in the simulations is the specification of gravity wave forcing at the lower boundary. The gravity wave model is based on the parameterization of *Lindzen* [1981] and modified by *Kiehl et al.* [1998]. We specify a uniform 10-mbar source in latitude and longitude at the lower boundary with six waves launched in each of the cardinal directions. With these boundary conditions and specified inputs for the parameterizations, all other physical and chemical processes are calculated self-consistently. The O_2 atmospheric band and atomic oxygen green line emission are calculated using the TIME-GCM determined fields and the formulation given by *McDade et al.* [1986].

[30] The TIME-GCM is first used to simulate a perpetual March equinox for conditions similar to the UARS measurements during March–April 1992–1993 as described by *McLandress et al.* [1996]. This is our base case. Difference fields are constructed from our perturbed cases described in the next section.

5.2. Simulated Airglow Patches

[31] Upon the base case described above, we specify regions that have enhanced gravity wave forcing at the lower boundary. The O_2 emission data clearly show regions of enhanced emissions over favored thunderstorm regions. In an attempt to model such enhancements we assume that enhanced gravity wave forcing at the lower boundary occurs in these regions. On 17 March, as shown in Figure 7, there are airglow enhancements observed over the Gulf of Mexico and southern United States, Africa, and Indonesia. In these regions the gravity wave forcing at the lower boundary of the model is enhanced above the background level. The enhanced gravity wave forcing is assumed to remain constant in time, and thus it interacts with the TIME-GCM diurnal cycle. The model run with the perturbed gravity wave forcing is compared to the base run by constructing difference fields of the perturbed model output minus the base model output. Figure 8 shows the difference fields calculated at the end of day 1 after the gravity wave flux in those regions was enhanced. Figure 8a shows the height-integrated O_2 emission rate and Figure 8b shows the regions of gravity wave enhancement as indicated by regions of enhanced eddy diffusion (regions in pink). These are also regions of strong downward vertical velocity.

[32] These TIME-GCM calculations show that the perturbations set up in a matter of a few hours and they are time-dependent because of the interaction of the gravity wave forcing with the mean winds and the diurnal cycle. Although not shown, the calculations show a vertical wave structure in temperature, zonal and meridional winds, and also in the zonal and meridional momentum forcing. The airglow emission rates and oxygen recombination are enhanced in regions of downward vertical velocity and suppressed in regions of upward vertical velocity. Vertical motion is clearly involved in the airglow perturbations in the model and dominates transport by vertical diffusion in regions of enhanced eddy mixing.

[33] In order to sample the region in a time-dependent manner similar to the way UARS observes the world, Figures 9a, 9b, and 9c show the vertical wind at 90-km altitude, the height-integrated O_2 emission rate, and the

height-integrated atomic oxygen recombination, all at a local solar time of midnight, over a two-day period. The plots show that the regions of enhanced O_2 emission are related to regions of enhanced gravity wave forcing. The model resolution is coarse, but clearly there is a good association between vertical velocity, O_2 integrated emission rate, and O recombination. Therefore the model supports the hypothesis that the regions of enhanced airglow are related to the distribution of gravity wave source strength and subsequent transmission through the background atmosphere. It also supports the argument that O_2 airglow enhancements are the direct result of strong enhancements in atomic oxygen recombination.

[34] These results do not depend significantly on the background dynamical conditions assumed. The equinox seasons of March/April 1992/1993 to which the model was tuned were periods in which the diurnal tide was very strong. Since the same tidal forcing was used in both the base and perturbed cases in this study, however, the exact tidal conditions assumed are of secondary importance. The strong variations with latitude and longitude shown in the difference fields (Figure 8) and in their temporal evolution (Figure 9) result solely from imposing a highly nonuniform gravity wave source distribution to interact with the mean winds and diurnal cycle. Under conditions of a significantly weaker diurnal tide or different background mean state than modeled here, the interaction of the enhanced gravity wave source regions with the mean winds and diurnal cycle could be expected to lead to a somewhat different time evolution from that shown in Figure 9, nevertheless the same relationship between the difference fields of vertical velocity, O_2 integrated emission rate, and O recombination would be maintained.

5.3. Global Implications of HRDI Measurements

[35] A very interesting implication of the HRDI high-resolution airglow observations is the fact that transport of atomic oxygen downward through the turbopause is not a steady or geographically uniform process. The extreme structure in the O_2 atmospheric band brightness implies that turbulence is very much a stochastic process, with transport over most of Earth being rather modest, but highly intense turbulence occurring in very limited and sporadic regions. The implication is that most of the downward transport of atomic oxygen occurs in these small regions which are appearing and disappearing at more or less random intervals. There are regions in which these turbulence occurrences are a regular event, such as over Central America, Africa, India, and Indonesia. It is probable that these intense turbulent events are driven by convective activity in the troposphere, by storms over orographic structures such as the high mountains, and other intense tropospheric sources of gravity waves. Over the rest of Earth there is a background of turbulence created by gravity wave activity that is generated by jet stream shear and other more ubiquitous atmospheric wave sources. This interpretation of mesospheric turbulence, if true, has profound implications on the way we must model the dynamical and chemical precesses that occur in this region. Models of the mesosphere in the past all used relatively uniform sources of gravity wave activity to produce smoothly varying turbulence at the mesopause. This results in relatively uniform wave acceleration of the winds in the mesosphere and implies that the global oxygen airglows are all relatively slowly varying functions of latitude, longitude, and time. As we have shown, however, the oxygen airglow is anything but uniform, and this means that the types of gravity wave activity which generate mesospheric turbulence must be modeled as relatively chaotic processes.

[36] In order to examine the implications of this model of gravity wave generation of mesospheric turbulence, we have introduced such a randomly varying gravity wave source into the TIME-GCM. The background wave source is taken to be a scaled-down source with the same smooth latitudinal structure as used previously, but most of the transport is produced by a random source of much greater intensity. This stochastic source of wave activity has been adjusted to produce a thermosphere that is in accord with the historic observations of atomic oxygen. In the new model results, we now see that the oxygen airglow is much more structured and exhibits behavior more nearly like what we have observed with HRDI. It is clear that more work will have to be done to create a wave source that will satisfy all of the previous observations of dynamics, chemistry, and thermodynamics of the mesopause and lower thermosphere. It is reasonable to expect that models of this portion of the atmosphere will indeed be improved by this improved description of the gravity wave activity.

6. Conclusions

[37] This paper has examined the global behavior of the nighttime O_2 atmospheric bands at the highest resolution ever reported. The results of this study are in accord with the early reports of brightness correlated with the tidal downwelling. The atmospheric bands are bright in the evening equatorial region where the (1,1) tide causes subsidence. The equatorial airglow dims after midnight when the tidal motion is reversed and the air moves upward. At midlatitudes the O_2 airglow is dim in the evening when the air is moving upward, but brightens in the morning when the tidal drift is downward. At higher latitudes there is a general brightening being caused by downwelling due to the meridional circulation. These general features are not uniformly distributed in longitude; large planetary-scale variations are observed. There is also extremely large variability seen at all observable scales. For the smaller regions we identified large enhancements in regions well known to exhibit intense convective activity in the tropics, and also in regions well known for planetary-scale wave activity, especially in the roaring 40s–60s in the Southern Hemisphere oceanic belt where frontal systems may be generating enhanced wave fluxes [*Charron and Manzini*, 2002]. The increased wave forcings are associated not only with enhanced source regions but are also found in regions of upper atmosphere winds that are favorable for vertical wave propagation [*Beres et al.*, 2002; *Liu and Hagan*, 1998; *McLandress et al.*, 2000]. These regions are dynamic and move from day to day and are intermittent [*Hickey and Walterscheid*, 2001] and can affect the airglow layers, such as OH [*Walterscheid and Schubert*, 1989], the O_2 atmospheric band and the oxygen green line. Strong gravity wave fluxes over an isolated thunderstorm region has also been reported by *Dewan et al.* [1998] from observations made by the MSX satellite.

[38] We suggest that the strong local variations in the O_2 atmospheric band emissions observed here at high spatial resolution are related to the fundamental quantity of gravity wave forcing of the mesosphere that is affected by both the source region and the favorable vertical transmission regions, and these data will be a useful diagnostic for improving models of the global dynamics of the mesosphere/lower thermosphere region.

[39] **Acknowledgments.** The work by members of the HRDI science team is sponsored by NASA through contract NAG5-11068. The National Center for Atmospheric Research is sponsored by the National Science Foundation. R. G. Roble acknowledges partial support from the NASA Sun-Earth Connection Theory Program. In addition, there have been contributions to the HRDI science program from a large number of people, including Alan R. Marshall, David A. Gell, and David A. Ortland who have made many helpful comments on our work.

References

Akmaev, R. A., and G. M. Shved, Modeling of the composition of the lower thermosphere taking account of the dynamics with applications to tidal variations of the [OI] 5577 Å airglow, *J. Atmos. Terr. Phys.*, *42*, 705–716, 1980.

Beres, J. H., M. J. Alexander, and J. R. Holton, Effects of tropospheric wind shear on the spectrum of convectively generated gravity waves, *J. Atmos. Sci.*, *59*, 1805–1823, 2002.

Brenton, J. G., and S. M. Silverman, A study of the diurnal variations of the 5577 Å [OI] airglow emissions at selected IGY stations, *Planet. Space Sci.*, *18*, 641–653, 1970.

Burrage, M. D., N. Arvin, W. R. Skinner, and P. B. Hays, Observations of the O_2 atmospheric band nightglow by the High-Resolution Doppler Imager, *J. Geophys. Res.*, *99*, 15,017–15,023, 1994.

Chamberlain, J. W., The formation of atmospheric O_2 emission in the airglow, *Astrophys. J.*, *119*, 328–333, 1954.

Charron, M., and E. Manzini, Gravity waves from fronts: Parameterization and middle atmosphere response in a general circulation model, *J. Atmos. Sci.*, *59*, 923–941, 2002.

Dewan, E. M., R. H. Picard, R. R. O'Neil, H. A. Gardiner, J. Gibson, J. D. Mill, E. Richards, M. Kendra, and W. O. Gallery, MSX satellite observations of thunderstorm-generated gravity waves in mid-wave infrared images of the upper stratosphere, *Geophys. Res. Lett.*, *25*, 939–942, 1998.

Donahue, T. M., B. Guenther, and R. J. Thomas, Spatial and temporal behavior of atomic oxygen determined by Ogo 6 airglow observations, *J. Geophys. Res.*, *79*, 1959–1964, 1974.

Dufay, J., and M. L. Tcheng, Recherches spectrophotometriques sur la lumière du ciel nocturne dans la région visible, *Ann. Géophys.*, *2*, 189–230, 1946.

Fleming, E. L., S. Chandra, M. R. Shoeberl, and J. J. Barnett, Monthly mean global climatology of temperature, wind, geopotential height, and pressure for 0–120 km, *NASA Tech. Memo. 100697*, 91 pp., NASA Goddard Space Flight Cent., Greenbelt, Md., Feb. 1988.

Forbes, J. M., Atmospheric tides: 1. Model description and results for the solar diurnal component, *J. Geophys. Res.*, *87*, 5222–5240, 1982a.

Forbes, J. M., Atmospheric tides: 2. The solar and lunar semidiurnal components, *J. Geophys. Res.*, *87*, 5241–5252, 1982b.

Fukuyama, K., Airglow variations and dynamics in the lower thermosphere and upper mesosphere. 1. Diurnal variation and its seasonal dependency, *J. Atmos. Terr. Phys.*, *38*, 1279–1287, 1976.

Grassl, H. J., W. R. Skinner, P. B. Hays, D. A. Gell, M. D. Burrage, D. A. Ortland, A. R. Marshall, and V. J. Abreu, Atmospheric wind measurements with the High-Resolution Doppler Imager, *J. Spacecr. Rockets*, *32*, 169–176, 1995.

Greer, R. G. H., E. J. Llewellyn, B. H. Solheim, and G. Witt, The excitation of $O_2(b^1\Sigma_g^+)$ in the nightglow, *Planet. Space Sci.*, *29*, 383–389, 1981.

Hagan, M. E., Comparative effects of migrating solar sources on tidal signatures in the middle and upper atmosphere, *J. Geophys. Res.*, *101*, 21,213–21,222, 1996.

Hagan, M. E., J. M. Forbes, and F. Vial, On modeling migrating solar tides, *Geophys. Res. Lett.*, *22*, 893–896, 1995.

Hays, P. B., V. J. Abreu, M. E. Dobbs, D. A. Gell, H. J. Grassl, and W. R. Skinner, The High-Resolution Doppler Imager on the Upper Atmosphere Research Satellite, *J. Geophys. Res.*, *98*, 10,713–10,723, 1993.

Hickey, M. P., and R. L. Walterscheid, Secular variations of OI 5577 Å airglow in the mesopause region induced by transient gravity wave packets, *Geophys. Res. Lett.*, *28*, 701–704, 2001.

Kasting, J. F., and R. G. Roble, A zonally averaged chemical-dynamical model of the lower thermosphere, *J. Geophys. Res.*, *86*, 9641–9653, 1981.

Kiehl, J. T., J. J. Hack, G. B. Bonan, B. A. Boville, D. L. Williamson, and P. J. Rasch, The National Center for Atmospheric Research Community Climate Model: CCM3, *J. Clim.*, *11*, 1131–1149, 1998.

Lindzen, R. S., Turbulence and stress due to gravity wave and tidal breakdown, *J. Geophys. Res.*, *86*, 9707–9714, 1981.

Liu, H.-L., and M. E. Hagan, Local heating/cooling of the mesosphere due to gravity wave and tidal coupling, *Geophys. Res. Lett.*, *25*, 2941–2944, 1998.

Liu, H.-L., R. G. Roble, M. J. Taylor, and W. R. Pendleton Jr., Mesospheric planetary waves at Northern Hemisphere fall equinox, *Geophys. Res. Lett.*, *28*, 1903–1906, 2001.

Marsh, D. R., W. R. Skinner, and V. A. Yudin, Tidal influences on O_2 atmospheric band dayglow: HRDI observations vs. model simulations, *Geophys. Res. Lett.*, *26*, 1369–1372, 1999.

McDade, I. C., D. P. Murtagh, R. G. H. Greer, P. H. G. Dickinson, G. Witt, J. Stegman, E. J. Llewellyn, I. Thomas, and D. B. Jenkins, ETON 2: Quenching parameters for the proposed precursors of $O_2(b^1\Sigma_g^+)$ and $O(^1S)$ in the terrestrial nightglow, *Planet. Space Sci.*, *34*, 789–800, 1986.

McLandress, C., G. G. Shepherd, B. H. Solheim, M. D. Burrage, P. B. Hays, and W. R. Skinner, Combined mesosphere/thermosphere winds using WINDII and HRDI data from the Upper Atmosphere Research Satellite, *J. Geophys. Res.*, *101*, 10,441–10,453, 1996.

McLandress, C., M. J. Alexander, and D. L. Wu, Microwave limb sounder observations of gravity waves in the stratosphere: A climatology and interpretation, *J. Geophys. Res.*, *105*, 11,947–11,967, 2000.

Murtagh, D. P., G. Witt, J. Stegman, I. C. McDade, E. J. Llewellyn, F. Harris, and R. G. H. Greer, An assessment of proposed $O(^1S)$ and $O_2(b^1\Sigma_g^+)$ nightglow excitation parameters, *Planet. Space Sci.*, *38*, 43–53, 1990.

Petitdidier, M., and H. Teitelbaum, $O(^1S)$ excitation mechanism and atmospheric tides, *Planet. Space Sci.*, *27*, 1409–1419, 1979.

Roble, R. G., Energetics of the mesosphere and thermosphere, in *The Upper Mesosphere and Lower Thermosphere*: *A Review of Experiment and Theory*, *Geophys. Monogr. Ser.*, vol. 87, edited by R. M. Johnson and T. L. Killeen, pp. 1–21, AGU, Washington, D. C., 1995.

Roble, R. G., On the feasibility of developing a global atmospheric model extending from the ground to the exosphere, in *Atmospheric Science Across the Stratopause*, *Geophys. Monogr. Ser.*, vol. 123, edited by D. E. Siskind, S. D. Eckermann, and M. E. Summers, pp. 53–67, AGU, Washington, D. C., 2000.

Roble, R. G., and E. C. Ridley, A thermosphere-ionosphere-mesosphere electro-dynamics general circulation model (TIME-GCM): Equinox solar cycle minimum simulations (30–500 km), *Geophys. Res. Lett.*, *21*, 417–420, 1994.

Roble, R. G., and G. G. Shepherd, An analysis of wind imaging interferometer observations of $O(^1S)$ equatorial emission rates using the thermosphere-ionosphere-mesosphere-electrodynamics general circulation model, *J. Geophys. Res.*, *102*, 2467–2474, 1997.

Shepherd, G. G., et al., WINDII: The Wind Imaging Interferometer on the Upper Atmosphere Research Satellite, *J. Geophys. Res.*, *98*, 10,725–10,750, 1993a.

Shepherd, G. G., et al., Longitudinal structure in atomic oxygen concentrations observed with WINDII on UARS, *Geophys. Res. Lett.*, *20*, 1303–1306, 1993b.

Shepherd, G. G., C. McLandress, and B. H. Solheim, Tidal influence on $O(^1S)$ airglow emission rate distributions at the geographic equator as observed by WINDII, *Geophys. Res. Lett.*, *22*, 275–278, 1995.

Shepherd, G. G., R. G. Roble, C. McLandress, and W. E. Ward, WINDII observations of the 558 nm emission in the lower thermosphere: The influence of dynamics on composition, *J. Atmos. Terr. Phys.*, *59*, 655–667, 1997.

Shepherd, G. G., R. G. Roble, S.-P. Zhang, C. McLandress, and R. H. Wiens, Tidal influence on midlatitude airglow: Comparison of satellite and ground-based observations with TIME-GCM predictions, *J. Geophys. Res.*, *103*, 14,741–14,751, 1998.

Shepherd, G. G., J. Stegman, P. Espy, C. McLandress, G. Thuillier, and R. H. Wiens, Springtime transition in lower thermospheric atomic oxygen, *J. Geophys. Res.*, *104*, 213–224, 1999.

Silverman, S. M., A note on the diurnal variation of the 5577 Å (OI) airglow emission, *Planet. Space Sci.*, *12*, 247–252, 1964.

Skinner, W. R., J.-H. Yee, P. B. Hays, and M. D. Burrage, Seasonal and local time variations in the $O(^1S)$ green line, O_2 atmospheric band, and OH Meinel band emissions as measured by the High Resolution Doppler Imager, *Adv. Space Res.*, *21*, 835–841, 1998.

Takahashi, H., Y. Sahai, B. R. Clemesha, P. P. Batista, and N. R. Teixeira, Diurnal and seasonal variations of the OH (8,3) airglow band and its correlation with OI 5577 Å, *Planet. Space Sci.*, *25*, 541–547, 1977.

Takahashi, H., Y. Sahai, and P. P. Batista, Tidal and solar cycle effects on the OI 5577 Å and OH(8,3) airglow emissions observed at 23°S, *Planet. Space Sci.*, *32*, 897–902, 1984.

Takahashi, H., P. P. Batista, Y. Sahai, and B. R. Clemesha, Atmospheric wave propagations in the mesopause region observed by the OH(8,3) band, NaD, O_2 A(8645 Å) band and OI 5577 Å nightglow emissions, *Planet. Space Sci.*, *33*, 381–384, 1985.

Taylor, M. J., M. B. Bishop, and V. Taylor, All-sky measurements of short period waves imaged in the OI(557.7 nm), Na(589.2 nm) and near infrared OH and O_2(0,1) nightglow emissions during the ALOHA-93 campaign, *Geophys. Res. Lett.*, *22*, 2833–2836, 1995.

Thomas, R. J., and T. M. Donahue, Analysis of Ogo 6 observations of the OI 5577-Å tropical nightglow, *J. Geophys. Res.*, *77*, 3557–3565, 1972.

Walterscheid, R. L., and G. Schubert, Gravity wave fluxes of O_3 and OH at the nightside mesopause, *Geophys. Res. Lett.*, *16*, 719–722, 1989.

Ward, F., and S. M. Silverman, Characteristics of the 5577 Å (OI) night airglow at Muruyama and its relation to magnetic activity, *J. Geophys. Res.*, *67*, 5357–5360, 1962.

Ward, W. E., Tidal mechanisms of dynamical influence on oxygen recombination airglow in the mesosphere and lower thermosphere, *Adv. Space Res.*, *21*, 795–806, 1998.

Ward, W. E., A simple model of diurnal variations in the mesospheric oxygen nightglow, *Geophys. Res. Lett.*, *26*, 3565–3568, 1999.

Ward, W. E., B. H. Solheim, and G. G. Shepherd, Two-day wave-induced variations in the oxygen green line volume emission rate: WINDII observations, *Geophys. Res. Lett.*, *24*, 1127–1130, 1997.

Yee, J.-H., and V. J. Abreu, Mesospheric 5577 Å green line and atmospheric motions-Atmospheric Explorer satellite observations, *Planet. Space Sci.*, *35*, 1389–1395, 1987.

Yee, J.-H., G. Crowley, R. G. Roble, W. R. Skinner, M. D. Burrage, and P. B. Hays, Global simulations and observations of O(^{1}S), O_2($^1\Sigma$) and OH mesospheric nightglow emissions, *J. Geophys. Res.*, *102*, 19,949–19,968, 1997.

Zhang, S. P., and G. G. Shepherd, The influence of the diurnal tide on the O(^{1}S) and OH emission rates observed by WINDII on UARS, *Geophys. Res. Lett.*, *26*, 529–532, 1999.

Zhang, S. P., R. G. Roble, and G. G. Shepherd, Tidal influence on the oxygen and hydroxyl nightglows: Wind Imaging Interferometer observations and thermosphere/ionosphere/mesosphere electrodynamics general circulation model, *J. Geophys. Res.*, *106*, 21,381–21,393, 2001.

P. B. Hays, Michigan Aerospace Corporation, 1777 Highland Drive, Suite B, Ann Arbor, MI 48109, USA. (hays@michiganaerospace.com)

J. F. Kafkalidis and W. R. Skinner, University of Michigan, 2455 Hayward St., Ann Arbor, MI 48109-2143, USA. (juliek@umich.edu)

R. G. Roble, NCAR, P.O. Box 3000, Boulder, CO 80307-3000, USA. (roble@hao.ucar.edu)